

## Projectile $Z$ dependence of Cu $K$ -shell vacancy production in 10-MeV/amu ion-solid collisions

R. L. Watson, J. M. Blackadar, and V. Horvat

*Cyclotron Institute and Department of Chemistry, Texas A&M University, College Station, Texas 77843*

(Received 28 December 1998)

The dependence of Cu (target atom)  $K$ -shell vacancy production cross sections on projectile atomic number was investigated in collision systems for which the ratio of projectile-to-target atomic numbers ( $Z_1/Z_2$ ) ranged from 0.34 to 2.86. A combination of energy and wavelength dispersive x-ray spectrometry was used to measure Cu  $K$  x-ray production cross sections and to determine the appropriate fluorescence yields for converting them to  $K$ -vacancy production cross sections. The high-resolution spectra also revealed the presence of sizable contributions from predominately single-ionization mechanisms not directly associated with ion-atom interactions. The role of electron capture to the projectile was examined by observing the dependence of the cross sections on target thickness. The Cu  $K$ -vacancy production cross sections determined for equilibrated projectiles display a plateau centered in the region of symmetric collisions ( $Z_1/Z_2 \sim 1$ ) and they become essentially constant beyond  $Z_1 = 54$ . The cross sections for  $Z_1 > 24$  fall far below a  $Z_1^2$  scaling law and are greatly overestimated by the perturbed stationary-state theory with energy loss, Coulomb deflection, and relativistic corrections. [S1050-2947(99)01110-5]

PACS number(s): 34.50.Fa

### I. INTRODUCTION

The accurate theoretical prediction of cross sections for electron excitation, ionization, and exchange has been a longstanding goal in the field of ion-atom collisions. Interest in this subject continues to inspire progress in the theoretical description of ionization mechanisms, as well as applications that require accurate databases of ionization cross sections. Extensive experimental and theoretical activity over the past three decades has led to a detailed understanding of target atom inner-shell vacancy production in light ion ( $Z_1 \leq 2$ ) collisions [1]. In the case of heavy-ion collisions, additional mechanisms, such as electron capture and (at low velocities) molecular-orbital promotion, must be taken into account. This, coupled with complexities pertaining to the presence of electrons on the projectile, causes both the theoretical description and the experimental investigation of inner-shell vacancy production in heavy-ion collisions to be challenging problems.

Most of the available experimental data for light ions, spanning a large range of relative velocities and target atomic numbers, are accurately described in a consistent way by a perturbed stationary-state theory with corrections for energy loss, Coulomb deflection, and relativistic effects [referred to as the (ECPSSR) theory] [2]. The development of an analytical method for including inner-shell vacancy production by electron capture to the projectile has extended the applicability of the ECPSSR theory to heavy ions [3]. Although reliable data for heavy ions is much less plentiful than for light ions, it is evident that the modified ECPSSR does a credible job of predicting target atom  $K$ -vacancy production cross sections over a remarkably large range of  $Z_1/Z_2$  (where  $Z_2$  is the target atomic number) and  $v_1/v_{2K}$  (where  $v_1$  is the velocity of the projectile and  $v_{2K}$  is the average velocity of the target  $K$  electron) [4–12]. The regions where reasonable agreement between theory and experiment have been demonstrated, as well as the locations of the present measurements, are shown in Fig. 1. Other mea-

surements with heavy-ion projectiles have been performed primarily in the low-velocity region where a molecular-orbital description is expected to apply [13].

Except for the high-velocity data of Anholt *et al.* [6] and the results of the present investigation, all of the other collision systems represented in Fig. 1 involve projectile ions having  $Z_1 \leq 18$ . Moreover, the region in the vicinity of  $v_1/v_{2K} = 1$  is unexplored beyond  $Z_1/Z_2 = 0.9$ . The present investigation was undertaken to examine the behavior of the  $K$ -vacancy production cross section in the intermediate velocity regime as  $Z_1/Z_2$  passes through unity and extends on

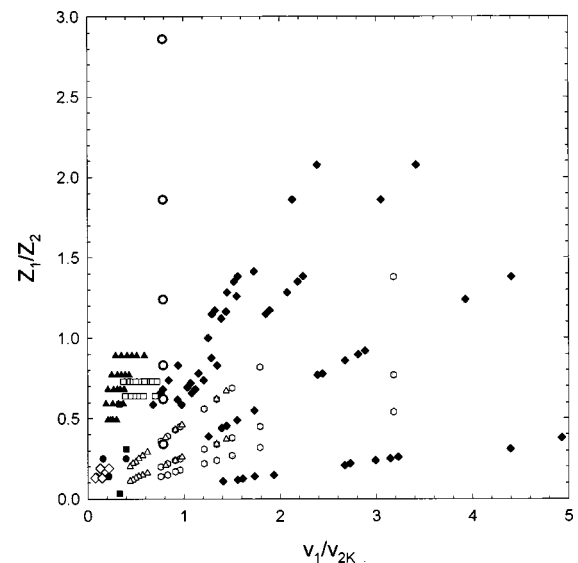


FIG. 1. Collision parameters of measured cross sections for  $K$ -shell vacancy production by heavy ions in which reasonable agreement with the predictions of the ECPSSR theory was demonstrated; filled circles, [4]; filled squares, [5]; filled diamonds, [6]; filled triangles, [7]; shaded hexagons, [9]; open triangles, [8]; open squares, [10]; and open diamonds, [12]. The coordinates of the present measurements are shown by the large open circles.

to very asymmetric collision systems where the projectile atomic number is much greater than that of the target. The primary goal of this paper is to establish the  $Z_1/Z_2$  boundary beyond which the ECPSSR theory begins to break down. The measurements were performed using 10-MeV/amu beams of Ne, Ar, Cr, Kr, Xe, and Bi incident on Cu targets. Target  $K$ -vacancy production cross sections were determined from the yields of Cu  $K$  x rays observed with a Si(Li) spectrometer. Copper was chosen as the target material because its  $K$  x rays fall in a favorable energy region, where there is minimum overlap with radiation from the projectiles and because it is available in a wide range of thicknesses.

Several rather formidable problems complicate the direct comparison of experiment with theory. One of them is associated with the fact that the ionic charges of the incident projectiles are generally much lower than their average equilibrium charges inside the target. This means that the most important electron-capture channels are initially closed. As the projectile enters the target, many of its electrons are stripped away and an equilibrium distribution of vacancy states quickly develops. During this equilibration process, target  $K$ -vacancy production by electron capture to the projectile can dramatically change. Therefore, the experimentally determined cross section is really a complicated average over target thickness [14];

$$\sigma(t) = \frac{1}{t} \int_0^t \sum_i f_i(x) \sigma_i dx, \quad (1)$$

where  $f_i$  and  $\sigma_i$  are the population fraction and  $K$ -vacancy production cross section, respectively, of each contributing projectile configuration  $i$ , and  $t$  is the target thickness. Two approaches have been explored in the present study. In the first, the cross sections were determined for a range of target thicknesses and extrapolated to zero thickness to obtain the direct-ionization cross sections. The second approach involved determining the cross sections for equilibrated projectiles and comparing them with the appropriate theoretical values calculated according to Eq. (1).

Another problem is associated with the fact that  $K$ -shell ionizing collisions of heavy ions simultaneously cause the ejection of many electrons from the  $L$  and higher shells of target atoms. This multiple ionization must be taken into account in calculating the fluorescence yield used to convert the  $K$  x-ray production cross sections to ionization cross sections. To facilitate this task, high-resolution spectral measurements with a crystal spectrometer were performed in order to accurately establish the numbers of  $L$ - and  $M$ -shell vacancies produced in the Cu targets by each of the different ion beams.

## II. EXPERIMENTAL METHODS

### A. Beams and targets

Beams of 10-MeV/amu Ne, Ar, Cr, Kr, Xe, and Bi were extracted from the Texas A&M K500 superconducting cyclotron and focused at the target position with the aid of a ZnS/CdS phosphor and a closed-circuit television camera. At this energy, beam particles from the cyclotron are delivered on target in pulses of approximately 2-ns duration and 100-ns separation. In the case of the x-ray yield measure-

TABLE I. Incident and estimated average equilibrium charges, and most probable equilibrium electron configurations of the ion beams.

Ion	Incident charge	Av. equilibrium charge	Configuration
Ne	4	9.6	bare
Ar	8	15.9	$1s^2$
Cr	10	20.4	$1s^2 2p^1$
Kr	17	28.8	$1s^2 2s^1 2p^3$
Xe	26	42.4	$1s^2 2s^2 2p^5 3p^1 3d^2$
Bi	35	65.3	$1s^2 2s^2 2p^6 3s^1 3p^2 3d^4$

ments, two 1-mm diameter collimators were inserted upstream from the target at distances of 1.5 and 6.0 cm to precisely define the beam spot. The incident charges of the ions, their estimated average equilibrium charges, and the most probable equilibrium electron configurations in Cu are listed in Table I. The latter two quantities were calculated using the ETACHA program of Rozet, Stéphan, and Vernhet [15].

The targets consisted of Cu evaporated onto 520- $\mu\text{g}/\text{cm}^2$  mylar backings and self-supporting Cu foils. Most of them were obtained from Goodfellow Inc. [16], but a few of the thicker foils were obtained from Chromium Corp. [17]. The thicknesses of the self-supporting foils were directly determined from measurements of their weights and areas, and they ranged from 0.97 to 4.67  $\text{mg}/\text{cm}^2$ . X-ray fluorescence was employed to determine the Cu thicknesses of the evaporated foils. Each of the targets was individually mounted behind the same beam-monitor target ( $\approx 20 \mu\text{g}/\text{cm}^2$  Se evaporated onto thin Mylar) in an x-ray fluorescence system and irradiated by a low-power Mo x-ray tube. The Cu and Se  $K$  x rays were observed by an Amptek Si-PIN photodiode detector [18] and their spectra were accumulated in a multi-channel analyzer. A calibration curve of the intensity ratio of the Cu-to-Se  $K\alpha$  peaks (corrected for absorption) versus Cu thickness was then constructed using the self-supporting foil targets and used to determine the thicknesses of the evaporated targets from their measured intensity ratios. The estimated precision of the target thicknesses, as determined by the above procedure, was  $\pm 8\%$  for thicknesses ranging from 6.7 to 200  $\mu\text{g}/\text{cm}^2$  and  $\pm 5\%$  for thicknesses ranging from 300 to 448  $\mu\text{g}/\text{cm}^2$ . Uncertainties in the thicknesses of the self-supporting foil targets were less than  $\pm 3\%$ .

### B. Energy-dispersive spectral measurements

A Si(Li) x-ray detector having an active area of 30  $\text{mm}^2$  and a resolution of 218 eV full width at half maximum (FWHM) at 8.04 keV (Cu  $K\alpha$ ) under the conditions of the experiment was positioned at  $90^\circ$  to the ion beam and viewed the target through a 0.025-mm thick Be window. The targets were mounted in an eight-position target wheel, which was driven remotely by a precision stepping motor and oriented at a  $45^\circ$  angle relative to both the beam axis and the Si(Li) detector axis. Projectile ions passing through the target were directly counted by a particle detector consisting of a 6.25- $\text{cm}^2 \times 0.32$ -cm block of BC-408 plastic scintillator mounted on a Hamamatsu R1927 photomultiplier tube. The

particle detector was located along the beam axis downstream from the target at a distance of 4.3 cm. A coincidence requirement was imposed on the x-ray and particle signals in order to eliminate any uncertainties concerning the efficiency of the particle detector. The counting rates in the particle detector ranged from  $2000 \text{ s}^{-1}$  (Bi ions) up to around  $50\,000 \text{ s}^{-1}$  (Ne ions), while the counting rates in the Si(Li) detector were always less than  $1000 \text{ s}^{-1}$ . As a check of the reliability of this method, several of the measurements were repeated using a chevron microchannel plate detector in place of the plastic scintillator/photomultiplier tube assembly. The results obtained with the two detector systems all agreed to within  $\pm 3\%$ .

The product of the Si(Li) detector efficiency  $\epsilon$  and solid angle fraction  $\Omega$  was measured using the 11.9, 13.9, 17.8, 20.8, 26.4, and 59.5-keV x-ray and  $\gamma$ -ray lines of a calibrated  $^{241}\text{Am}$  source. These calibration points were then fit to the standard efficiency model function for a Si(Li) detector;

$$\epsilon = e^{-a_1}(1 - e^{-a_2}), \quad (2)$$

where

$$a_1 = \sum_i \mu_i t_i$$

and

$$a_2 = \mu_{\text{Si}} t_{\text{Si}}.$$

In the above expression for  $a_1$ , the sum extends over the product of the total mass absorption coefficient  $\mu$  and thickness  $t$  for the Be window, the Au layer, and the Si dead layer. The  $a_2$  term involves the product of the Si photoabsorption coefficient and depletion region thickness. In the fitting procedure, the unknown thicknesses of the Au layer, Si dead layer, and depletion region were treated as fitting parameters. Efficiency values needed in the data analysis were calculated with the model function and are believed to have an uncertainty of no more than  $\pm 3\%$  over the region of the Cu  $K$  x rays.

Typical x-ray spectra obtained in the present study are shown in Fig. 2. The Cu  $K\alpha$  and  $K\beta$  x-ray peaks are prominently displayed near the center of each spectrum. The dashed lines show the diagram line energies of the  $K\alpha_{1,2}$  and  $K\beta_{1,3}$  transitions in singly ionized Cu atoms. Multiple ionization of the  $L$  and  $M$  shells causes these peaks to broaden and shift to higher energies with increasing severity as the projectile atomic number increases. A shoulder on the high energy side of the  $K\alpha$  peak is caused by the  $K\alpha$  hypersatellites, which originate from  $2p$  to  $1s$  transitions in Cu atoms having double  $K$  vacancies. The other peaks visible in Fig. 2 are caused by x rays from the projectile or by pulse pileup.

### C. Wavelength-dispersive spectral measurements

A 12.7-cm Johansson-type curved crystal spectrometer was mounted on a specially designed vacuum chamber with its focal circle oriented perpendicular to the beam axis. It viewed the target, which was tilted at a  $45^\circ$  angle relative to both the beam axis and the spectrometer axis, from above. The spectrometer was equipped with a LiF diffraction crystal

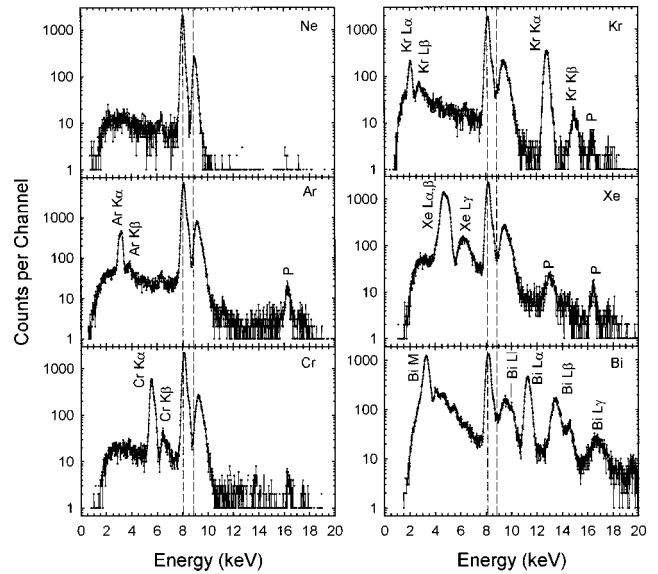


FIG. 2. X-ray spectra excited by 10-MeV/amu projectiles passing through a  $965\text{-}\mu\text{g}/\text{cm}^2$ -thick Cu foil, measured with a Si(Li) spectrometer. The dashed lines indicate the positions of the Cu  $K\alpha$  and  $K\beta$  (single vacancy) diagram lines. The peaks labeled  $P$  are caused by pulse pileup.

and a flow proportional counter (10% methane and 90% argon at 1 atm). Further details of the spectrometer system are given in Ref. [19].

Scans of the Cu  $K$  x-ray region were performed in second order for all of the self-supporting foil targets. Unfortunately, the beam intensities required for the high-resolution measurements were too high to use on the evaporated targets with mylar backings. The resolution obtained for the Cu  $K\alpha_1$  line was 12 eV (FWHM). Typical spectra are shown in Fig. 3. The first two peaks in each spectrum contain the  $K\alpha_2$  and

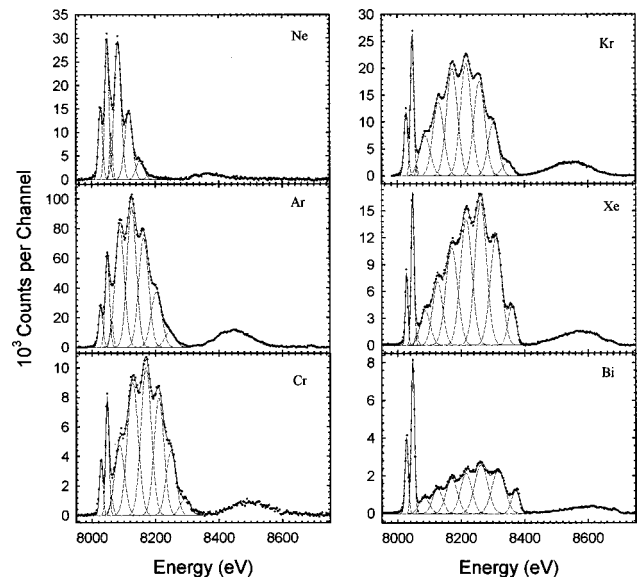


FIG. 3. Cu  $K\alpha$  x-ray spectra excited by 10-MeV/amu projectiles passing through a  $2.57\text{-mg}/\text{cm}^2$ -thick Cu foil, measured in second order with a curved crystal spectrometer. The fitted portions of the spectra contain the  $K\alpha_{1,2}$  doublet and the  $K\alpha L^n$  satellites. The broad peaks to the right of the satellites contain the unresolved  $K\alpha$  hypersatellites.

$K\alpha_1$  lines originating from initial states having one  $K$  vacancy and zero  $L$  vacancies, while the other peaks in the fitted portion of each spectrum contain the  $K\alpha$  satellite lines originating from initial states having one  $K$  vacancy and one to seven  $L$  vacancies. The broad peak above the  $K\alpha$  satellite region (which appears as a shoulder on the  $K\alpha$  peak in Fig. 2) contains the  $K\alpha$  hypersatellites. It is readily seen from the changes in the  $K\alpha$  satellite intensity distribution that the degree of multiple ionization increases considerably in going from Ne projectiles to Bi projectiles. Another noteworthy feature of the spectra shown in Fig. 3 is the rapid increase in the intensity of the  $K\alpha_{1,2}$  peaks relative to the  $K\alpha$  satellite peaks as the projectile atomic number increases. This behavior suggests that other mechanisms besides those associated with excitation, ionization, and capture by the projectile contribute to the production of states with single  $K$  and zero  $L$  vacancies.

Energy calibration was accomplished by recording spectra of ion-excited  $K$  x rays in targets containing Ca and Mn, and  $L$  x rays in a target containing Sb. In addition to the multiple-vacancy satellite peaks, the (single-vacancy) diagram lines also were clearly visible in these spectra, presumably due to the same single-vacancy production mechanism(s) referred to above. The energy calibration utilized the  $K\alpha_{1,2}$  and  $K\beta_{1,3}$  peaks of both Ca and Mn, as well as the  $L\alpha$ ,  $L\beta_1$ , and  $L\beta_{2,15}$  peaks of Sb. The Cu  $K\alpha_2$ ,  $K\alpha_1$ , and  $K\beta_{1,3}$  peaks provided three more (internal) calibration points for each Cu spectrum at energies of 8027.85, 8047.83, and 8905.42 eV, respectively [20].

### III. ANALYSIS AND RESULTS

#### A. $K\alpha$ satellite spectra

The primary purpose of the high-resolution measurements was to determine the average target-atom  $L$ - and  $M$ -shell vacancy configurations produced in  $K$  x-ray producing collisions of the various projectiles so that accurate fluorescence yields could be computed for use in converting the measured x-ray yields to vacancy-production cross sections. To accomplish this objective, the portions of the high-resolution spectra containing the  $K\alpha$  satellites were analyzed by means of a least-squares-fitting procedure in which the  $K\alpha_{1,2}$  peaks and each satellite peak were represented by Gaussians, as is illustrated in Fig. 3. The centroid energies of the satellite peaks directly reflect both the number of  $L$  and  $M$  vacancies, and since the number of  $L$  vacancies is already known, the number of  $M$  vacancies can be inferred by comparing the measured energies to theoretical transition energies averaged over the various possible configurations for specified  $L$ - and  $M$ -shell populations. The experimental average  $K\alpha$  satellite energies (measured relative to the  $K\alpha_1$  diagram line energy) obtained with the different projectiles are compared in Fig. 4. The number of  $M$  vacancies associated with the lower-order satellite peaks (i.e.,  $n = 1$  to 4) apparently increases rapidly at low  $Z_1$ , but levels off beyond  $Z_1 \approx 24$ . The average numbers of  $M$  vacancies deduced by comparing the measured satellite energies with the results of Dirac-Fock calculations performed with the Desclaux program [21] are given in Table II.

The  $K\alpha$  satellite intensities were obtained from the least-squares fits and corrected for proportional counter efficiency

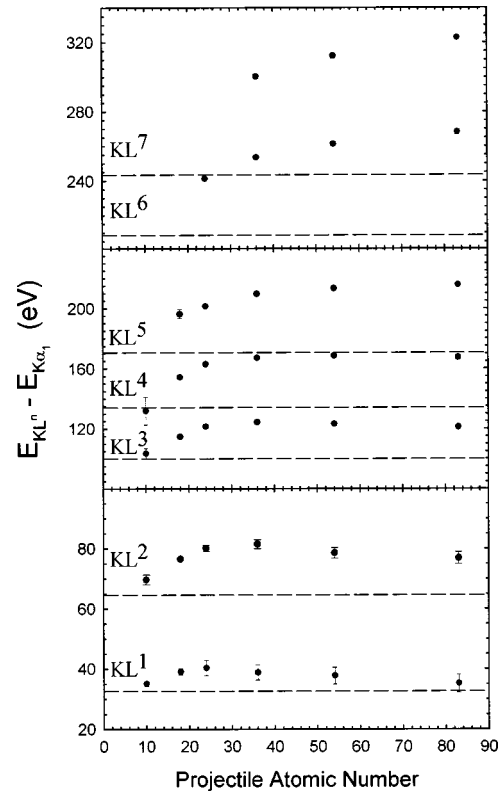


FIG. 4. Average energies of the  $K\alpha$  satellite peaks relative to the energy of the  $K\alpha_1$  diagram line (8047.83 eV) as a function of the projectile atomic number. The dashed lines indicate the energies given by the Dirac-Fock program of Desclaux [21] for Cu atoms having zero  $M$ -shell vacancies.

and absorption in the target. Variation of the crystal reflectivity was assumed to be negligible over the range of energy involved. Based on numerous previous studies of  $K$  x-ray spectra excited by ion impact, the relative intensities of the  $K\alpha$  satellites are expected to approximate binomial distributions. Therefore, the observation that the intensities of the  $KL^0$  peaks are greatly enhanced over those predicted by a binomial fit to the satellite peaks in the spectra obtained with Cr, Kr, Xe, and Bi projectiles (see Fig. 3) is strong evidence that other mechanisms besides those associated with direct interactions between the projectile nucleus and target electrons contribute to the production of  $K$  x rays from singly ionized target atoms. As has been pointed out in several previous investigations [22–24], photoionization of target atoms by projectile x rays and by ion-excited target  $K\beta$  x rays that are shifted above the  $K$  binding energy due to multiple ionization is a plausible mechanism for  $KL^0$  enhancement. Another possible source of  $KL^0$  x rays is electron-impact ionization caused by secondary electrons produced in the ion-atom collisions.

It was necessary to correct the x-ray yields measured with the Si(Li) detector system for contributions from these other mechanisms in order to obtain reliable cross sections for vacancy production by direct ion-atom interactions. Therefore, the thickness dependence of this effect was investigated and compared with predictions of the calculated  $KL^0$  enhancements expected from photoionization. The ion-induced con-

TABLE II. The average numbers of  $M$  vacancies deduced from the average  $K\alpha$  satellite energies. (The uncertainties in these numbers are estimated to be  $\pm 1$  electron.)

Projectile atomic number	$KL^1$	$KL^2$	$KL^3$	$KL^4$	$KL^5$	$KL^6$	$KL^7$
10	1.0	1.8	1.1	0			
18	2.6	4.4	4.8	5.9	6.8		
24	3.1	5.6	7.0	8.5	8.1	7.8	
36	2.5	6.1	7.9	9.7	10.3	10.7	12.4
54	2.1	5.1	7.6	10.1	11.3	12.6	15.0
83	1.0	4.5	6.9	9.8	11.9	14.2	17.3

tribution to the  $KL^0$  peak of each high-resolution spectrum was estimated by first fitting a binomial distribution to the satellite intensities to obtain the best value of the average  $L$ -vacancy probability  $p_L$ . The binomial intensity  $I_{\text{bin}}(n)$  of a  $KL^n$  peak is given by

$$I_{\text{bin}}(n) = P(n)I_{K\alpha}, \quad (3)$$

where  $I_{K\alpha}$  is the total  $K\alpha$  x-ray intensity corrected for  $KL^0$  enhancement (i.e.,  $I_{K\alpha} = I_{\text{tot}} - I_E$ ), and

$$P(n) = \binom{8}{n} p_L^n (1 - p_L)^{8-n}. \quad (4)$$

The binomial intensity for  $n=0$  [ $I_{\text{bin}}(0)$ ] was taken to be the  $KL^0$  peak intensity associated with the ion-induced contribution. It is given by the following expression:

$$I_{\text{bin}}(0) = \frac{P(0)}{1 - P(0)} [I_{\text{tot}} - I_{\text{obs}}(0)], \quad (5)$$

in which  $I_{\text{obs}}(0)$  is the observed intensity of the  $KL^0$  peak. Finally, the relative enhancement of the  $KL^0$  peak, defined as

$$R_E = \frac{I_{\text{obs}}(0) - I_{\text{bin}}(0)}{I_{\text{tot}}}, \quad (6)$$

was calculated and used to examine the dependence of the enhancement effect on projectile atomic number and target thickness.

Figure 5 shows a comparison of the observed  $K\alpha$  satellite relative intensities with those obtained from the fitted binomial distributions. The close correspondence between the two intensity distributions for each of the projectiles lends credence to the method. The dependence of the average  $L$ -vacancy probability on the projectile atomic number is shown in Fig. 6. Also shown in this figure are the estimated  $p_L$  values for the original vacancy distributions created at the time of collision. They were calculated by taking into account the fractions of  $L$  vacancies filled by radiative and Auger transitions from the  $M$  shell prior to  $K$ -vacancy decay using a procedure that is outlined in Sec. III B. As may be seen from this figure, the  $p_L$  values that characterize the initial vacancy distributions are on average about 10% higher than those that characterize the observed x-ray satellite distributions.

In considering the possible sources of the observed  $KL^0$  enhancements, it is readily apparent from the spectra shown in Fig. 2 that photoionization is a prime candidate. The large energy shift displayed by each  $K\beta$  peak means that in all

cases substantial intensities of x rays are produced with energies just above the Cu  $K$  absorption edge, where the  $K$ -shell photoionization cross section has its maximum value. Furthermore, x rays emitted by some of the projectiles (specifically Kr  $K$  x rays and Bi  $L$  x rays) have significant cross sections for photoionizing Cu  $K$  electrons. The role of photoionization was investigated by performing calculations of the expected  $KL^0$  relative enhancement based on the observed intensities of Cu  $K\beta$  x rays emitted above the absorption edge and (in the pertinent cases) the observed intensities of projectile x rays. The details of the calculations are given in the Appendix. The results are shown in Figs. 7 and 8. In Fig. 7, the measured and calculated  $KL^0$  relative enhancements

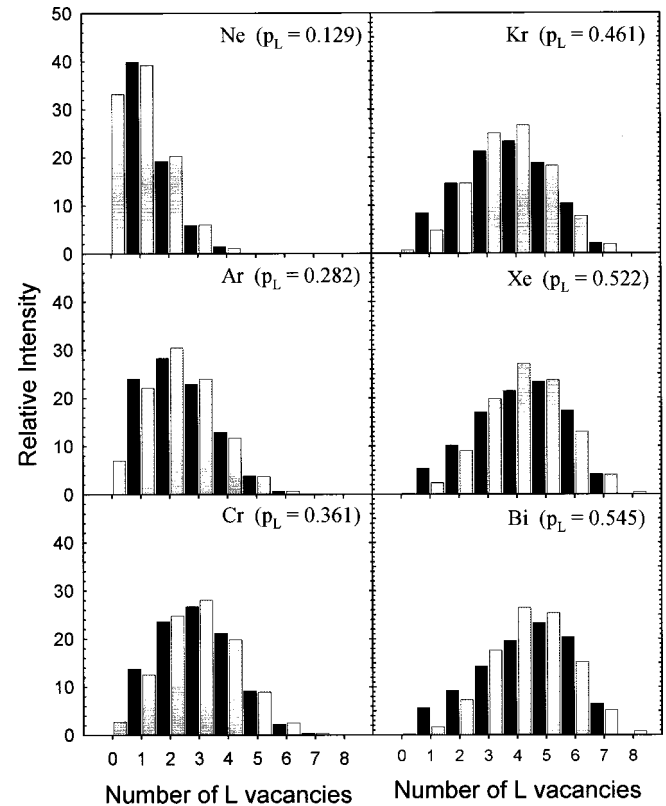


FIG. 5. Comparison of the measured  $K\alpha$  satellite intensities (black bars) with those calculated assuming a binomial distribution (shaded bars) having the average  $L$ -vacancy probability given in the upper right-hand corner of each frame. The measured intensities have been corrected for detector efficiency and absorption. The measured  $KL^0$  intensities (not shown) were excluded from the fitting procedure used to determine the  $p_L$  values because they contained contributions from secondary excitation processes.

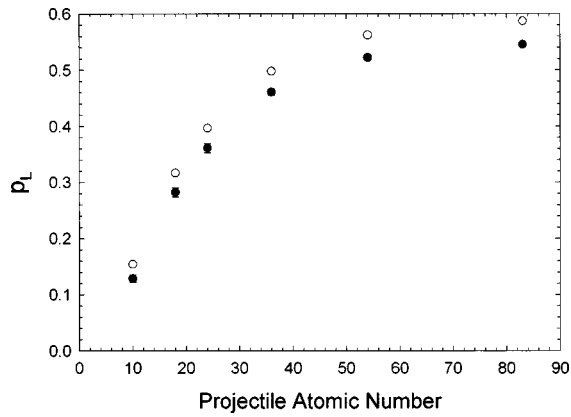


FIG. 6. The average  $L$ -vacancy probabilities obtained from binomial fits to the  $K\alpha$  x-ray satellite intensity distributions (filled circles) and the calculated average  $L$ -vacancy probabilities for the initial  $L$ -vacancy distributions formed at the time of collision (open circles).

for a target thickness of  $2.57 \text{ mg/cm}^2$  are plotted as a function of the projectile atomic number. The apparent dip in the data at  $Z_1=54$  is caused by the additional contributions to  $R_E$  from projectile x rays at the two neighboring points  $Z_1=36$  (Kr) and  $83$  (Bi). Within experimental errors, the relative enhancements observed for Ne, Ar, and Cr projectiles are fully accounted for by  $K\beta$  photoionization. However, the relative enhancements observed for the Kr, Xe, and Bi projectiles are considerably larger than those predicted for photoionization alone. Since the reliability of the calculations is expected to be of the order of  $\pm 10\%$ , it must be concluded that another mechanism produces substantial additional contributions to the  $KL^0$  x-ray intensity. As mentioned above, the most likely candidate is  $K$ -shell ionization by secondary electrons. It is well known, for example, that binary-encounter electrons are produced with energies peak-

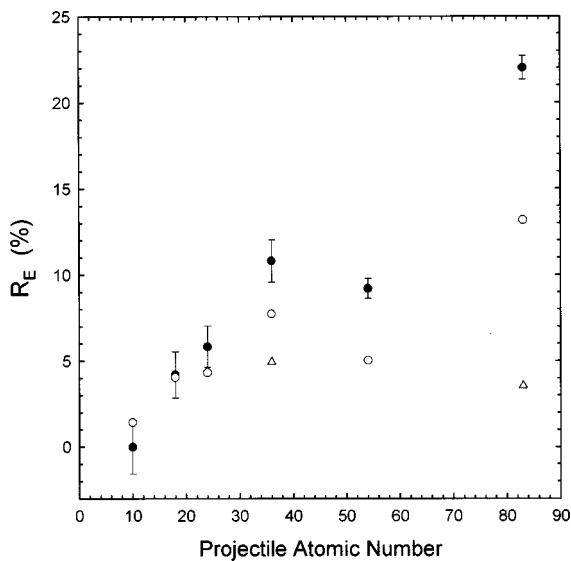


FIG. 7. Comparison of the experimental (filled circles) and calculated (open circles) relative enhancements for a  $2.57\text{-mg/cm}^2$ -thick Cu foil. The calculated contributions to the relative enhancements for  $Z_1=36$  and  $83$  from fluorescence by projectile (Kr  $K$  and Bi  $L$ ) x rays are shown by the open triangles.

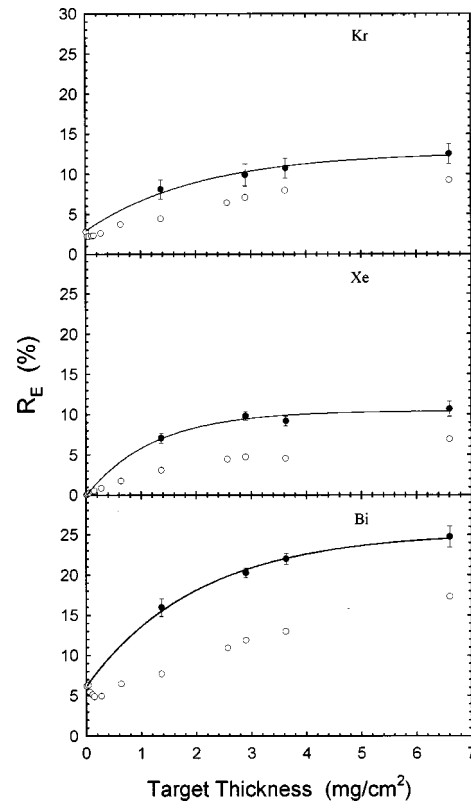


FIG. 8. Target-thickness dependence of the relative enhancement for Kr, Xe, and Bi projectiles. (Filled circles are experimental and open circles are calculated.) The curves show the results of least-squares fits to the experimental points (see text).

ing around  $4mE/M$  at zero degrees, where  $m$  is the mass of the electron, and  $M$  and  $E$  are the mass and energy of the projectile, respectively. For  $10\text{-MeV/amu}$  projectiles, the peak energy is  $22 \text{ keV}$  which is  $2.5$  times larger than the Cu  $K$ -binding energy. Moreover, cross sections for ionization by electron impact are comparable to those for photoionization. Although it is difficult to calculate the expected contribution from secondary electrons with much certainty, preliminary estimates are of the right order of magnitude and reproduce the observed dependence on projectile atomic number and target thickness. More accurate calculations will require the incorporation of a model for electron transport in solids and a better way of accounting for electron energy loss and target surface effects.

The target-thickness dependence of the  $KL^0$  relative enhancement is shown in Fig. 8 for Kr, Xe, and Bi projectiles. In the cases of Kr and Bi, the predicted photoionization relative enhancement does not go to zero at zero target thickness because of contributions from projectile x rays produced in the target backing. It was found that the measured relative enhancements were well represented by the empirical fitting function

$$R_E = a + b(1 - e^{-ct}), \quad (7)$$

where  $a$ ,  $b$ , and  $c$  are fitting parameters and  $t$  is the target thickness. The results of fits with this function shown by the solid lines in Fig. 8 were used to correct the measured  $K\alpha$  x-ray yields in the cross section determinations for Kr, Xe,

and Bi projectiles. The relative enhancements used to correct the x-ray yields for Ne, Ar, and Cr were the ones calculated for photoionization.

### B. K-vacancy production cross sections

A least-squares peak-fitting analysis was performed on each of the spectra obtained with the Si(Li) detector system to accurately determine the intensities and energies of the various x-ray components. In fitting the Cu  $K\alpha$ ,  $K\alpha$  hypersatellites, and  $K\beta$  were each represented by a separate Gaussian. The Cu  $K\alpha$  intensities were then corrected for  $KL^0$  enhancement;

$$I_{K\alpha} = I_{\text{tot}}(1 - R_E). \quad (8)$$

Division of the corrected  $K\alpha$  intensities by the number of detected ions and correction for absorption in the target and Si(Li) detection probability yielded  $N_{K\alpha}$ , the total number of  $K\alpha$  x rays produced by ion-atom interactions per particle. The total number of  $K$  vacancies produced per particle is given by

$$N_K = \frac{N_{K\alpha}}{\bar{\omega}_{K\alpha}}, \quad (9)$$

where  $\bar{\omega}_{K\alpha}$  is the average  $K\alpha$  fluorescence yield.

The average fluorescence yields required in Eq. (9) were calculated by an iterative procedure in which the first step involved estimation of the  $p_L$  value characterizing the initial  $L$ -vacancy distribution. Then, assuming the  $L$  electrons were distributed statistically among the  $L$  subshells and the  $M$ -shell population fractions were the same as those for the  $L$  shell, the population fractions of all configurations formed by allowed radiative and Auger transitions from the  $L$  and  $M$  shell to the  $K$  shell and from the  $M$  shell to the  $L$  shell were computed, yielding a second-generation population distribution. Theoretical (single-vacancy) transition rates [25,26] corrected for the number of vacancies by the scaling procedure of Larkins [27] were employed in this step. The evolution of the population distribution was followed by repeating the above procedure until the total numbers of  $K\alpha$  and  $K\beta$  x rays arising from each  $L$ -vacancy configuration and the average numbers of  $M$  vacancies for each x-ray satellite had been determined. These numbers were then used to calculate the average  $K\alpha$  and  $K\beta$  fluorescence yields, and the  $p_L$  value of the final  $K\alpha$  x-ray distribution. Finally, the calculated x-ray distribution  $p_L$  value was compared with the measured one and if it did not agree, a new initial  $L$ -vacancy distribution was generated and the whole process was repeated.

It was found that the assumption of an initial statistical population of the  $M$  shell resulted in predicted  $K\beta$  to  $K\alpha$  intensity ratios that did not agree with those observed experimentally, as is shown in Fig. 9. The experimental ratios for heavy-ion collisions are much higher than the single vacancy (photoionization) value, which indicates that the average  $3p$ -electron populations must be larger than the average  $2p$ -electron populations. On the other hand, if a smaller number of  $M$  vacancies in the initial vacancy distribution is assumed, the calculated average number of  $M$  electrons in the final state for each satellite is too large to explain the

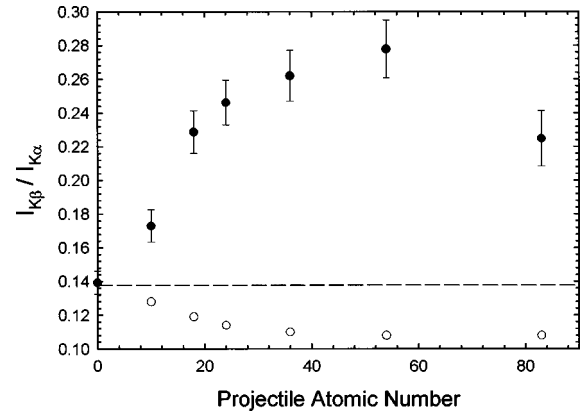


FIG. 9. The Cu  $K\beta$  to  $K\alpha$  intensity ratio as a function of the projectile atomic number. The filled circles are the measured intensity ratios and the open circles are intensity ratios calculated assuming the  $L$  and  $M$ -shell populations produced in the collisions are statistically distributed among the subshells. The experimental data point at  $Z_1=0$  is for photoionization and was measured by fluorescing a copper target with x rays and  $\gamma$  rays from an  $^{241}\text{Am}$  source. The dashed line shows the theoretical value of Scofield [25] for singly ionized atoms.

energy shifts of the satellite peaks. This strongly suggests that the initial vacancy distribution is not statistically populated and that in particular, the  $3p$  orbitals contain more electrons than expected. A possible rationale for this might be that the  $3p$  orbitals are continuously being filled from the conduction band. The final calculations were carried out under the assumption that the  $3p$  orbitals are preferentially populated because this assumption yielded ratios of the average  $K\beta$  and  $K\alpha$  fluorescence yields that were in good agreement with the measured  $K\beta$ -to- $K\alpha$  intensity ratios.

Total  $K$ -shell vacancy production cross sections are shown in Fig. 10 as a function of target thickness. The error bars include contributions associated with uncertainties in the target thickness, Si(Li) detection probability, measured

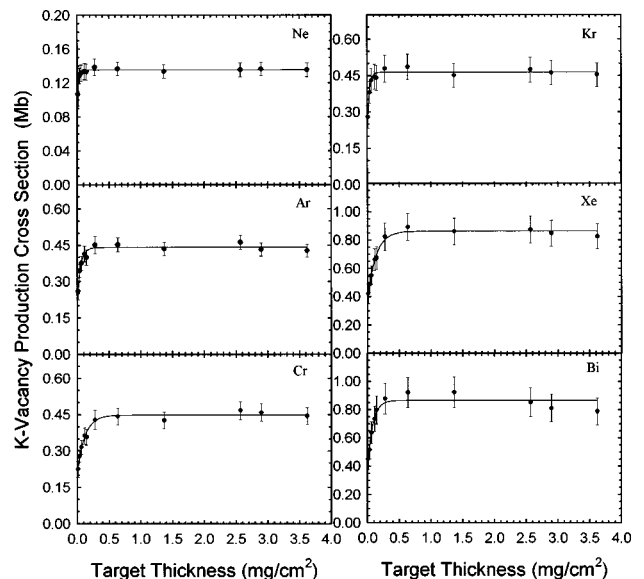


FIG. 10. Target-thickness dependence of the Cu  $K$ -shell vacancy production cross sections. The curves show the results of least-squares fits using the empirical function given in the text.

TABLE III. Average Cu  $K\alpha$  fluorescence yields,  $K$ -shell vacancy production cross sections in Mb (where  $\sigma_0$  is the zero-thickness cross section,  $\sigma_C$  is the thickness-averaged electron-capture cross section, and  $\sigma_{eq}$  is the total cross section for equilibrated projectiles), and equilibration thicknesses ( $\mu\text{g}/\text{cm}^2$ ).

$Z_1$	$\bar{\omega}_{K\alpha}$	$\sigma_0$	$\sigma_C$	$\sigma_{eq}$	$t_{eq}$
10	0.411	$0.082 \pm 0.020$	$0.053 \pm 0.013$	$0.136 \pm 0.008$	78
18	0.445	$0.233 \pm 0.033$	$0.208 \pm 0.029$	$0.440 \pm 0.025$	249
24	0.468	$0.215 \pm 0.025$	$0.233 \pm 0.028$	$0.448 \pm 0.031$	552
36	0.501	$0.206 \pm 0.041$	$0.257 \pm 0.052$	$0.463 \pm 0.043$	142
54	0.523	$0.379 \pm 0.051$	$0.484 \pm 0.065$	$0.855 \pm 0.081$	608
83	0.530	$0.373 \pm 0.060$	$0.592 \pm 0.079$	$0.847 \pm 0.095$	364

$K\alpha$  x-ray yield per particle, fluorescence yield, and  $KL^0$  relative enhancement. As expected, in each case the cross section at first increases rapidly with increasing target thickness and then levels off. This behavior is caused by a variation of the cross section for  $K$ -vacancy production via electron capture to the projectile. As the projectile enters the target, its electrons are rapidly stripped away, opening new electron-capture channels, until an equilibrium population distribution is established. The curves in Fig. 10 show the results of least-squares fits using the empirical fitting function

$$\sigma_K = \sigma_0 + \sigma_C(1 - e^{-at}), \quad (10)$$

where  $\sigma_0$  and  $\sigma_C$  represent the zero-thickness (predominately direct-ionization) cross sections and the thickness-averaged total-capture cross sections, respectively. This fitting function reproduces the trend of the data quite well and it provides a reasonable means of extrapolation to obtain the zero-thickness cross sections. The values of  $\sigma_0$  and  $\sigma_C$  determined in this analysis and the average  $K\alpha$  fluorescence yields used in Eq. (9) are given in Table III. Also listed in Table III are  $\sigma_{eq}$  the  $K$ -vacancy production cross sections for equilibrated projectiles, and  $t_{eq}$ , defined as the target thicknesses at which the exponential term in Eq. (10) has reached a value of 0.01. The values of  $\sigma_{eq}$  were determined by averaging the total  $K$ -vacancy production cross sections for target thicknesses greater than  $600 \mu\text{g}/\text{cm}^2$ . They are within  $\pm 1\%$  of the values obtained by adding  $\sigma_0$  and  $\sigma_C$ .

#### IV. COMPARISON WITH THEORY

Theoretical cross sections for Cu  $K$ -shell vacancy production by 10-MeV/amu projectiles are presented in Fig. 11. The cross sections were calculated within the framework of the ECPSR theory and include contributions from direct  $K$ -shell ionization [2] and  $K$ -electron capture to the projectile [3]. For the purposes of illustration, calculation of the electron-capture contribution, which depends on the electronic configuration of the projectile, were performed both for bare projectiles and for equilibrated projectiles in their electronic ground states. The latter choice was selected to demonstrate the effect of electrons attached to the projectile.

For comparison with the present experimental results, electron-capture cross sections averaged over target thickness were computed. These calculations required knowledge of how the distribution of projectile electronic configurations evolves with target thickness. This information was obtained

by means of the program ETACHA written by Rozet, Stéphan, and Vernhet [15]. Program ETACHA solves the rate equations for the population fractions of all projectile configurations involving up to 28 electrons distributed over subshells having principal quantum numbers equal to 1, 2, and 3, using theoretical cross sections for electron capture, ionization, and excitation, and scaled radiative and Auger decay rates. The code was modified to provide the additional output needed for the current application. The number of contributing configurations included in the calculations depended on the projectile, but in all cases they accounted for 99.9% of the total population. For example, with Xe projectiles the number of contributing configurations included reached 3500 at a target thickness of  $100 \mu\text{g}/\text{cm}^2$ . Binding energies for electrons captured into each of the contributing projectile configurations were obtained using the Dirac-Fock program of Desclaux [21].

The experimental and theoretical direct-ionization and total-capture cross sections are compared in Fig. 12. As indicated above, the theoretical electron-capture cross sections were averaged over target thickness in accordance with Eq. (1). This average value increases well beyond the equilibrium thickness until the contribution from the preequilibrium phase becomes negligible. However, before reaching this

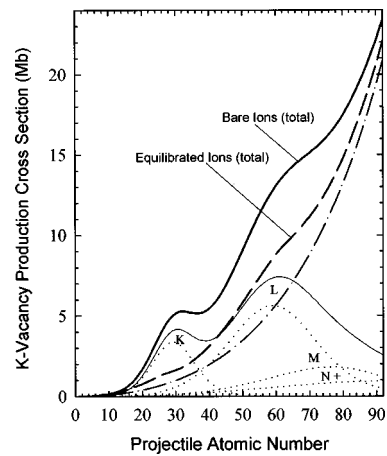


FIG. 11. Theoretical (ECPSR)  $K$ -shell vacancy production cross sections for bare ions (where the thick solid curve is the total cross section, the dot-dashed curve is the direct ionization cross section, and the thin solid curve is the total electron-capture cross section) and for projectiles with equilibrium charges and ground-state electron configurations (dashed curve). The cross sections for target  $K$ -electron capture to various shells of bare projectile are shown by the dotted curves.

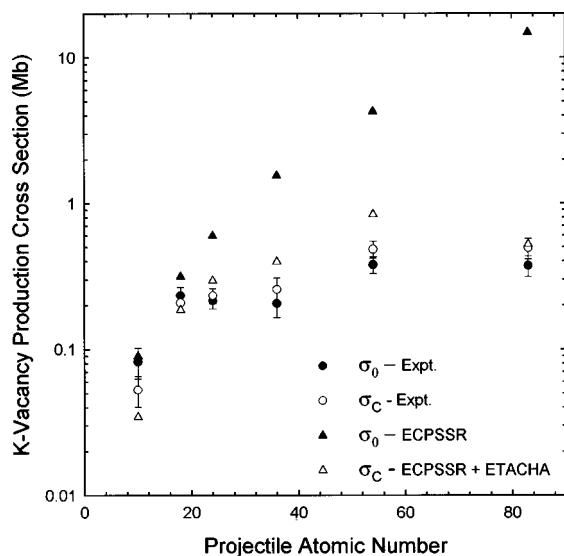


FIG. 12. Comparison of the experimental zero-thickness cross sections  $\sigma_0$  and total-capture cross sections  $\sigma_C$  with theoretical (ECPSSR) cross sections for direct ionization and  $K$ -electron capture. In the case of capture, the cross sections for the most probable electron configurations of the projectile (as determined using ETACHA) were averaged over target thickness.

point, the cross sections for equilibrated projectiles may have started to decrease due to projectile energy loss. In these cases, the total-capture cross sections shown in Fig. 12 are the maximum values of the averages over target thickness. It is evident that the direct-ionization cross sections are in good agreement for Ne and Ar projectiles, but beyond Ar, the theoretical cross sections quickly rise above the experimental cross sections. The total-capture cross sections, on the other hand, display rather good agreement with each other over the whole range of projectiles. It should be noted that the theoretical  $\sigma_C$  rely on both the electron-capture formulation in the ECPSSR and the configuration distributions predicted by ETACHA, while the theoretical  $\sigma_0$  depend only on the validity of the ECPSSR description of direct ionization.

The  $K$ -shell vacancy production cross sections for equilibrated projectiles are plotted in Fig. 13. The measured cross sections display a plateau centered in the region around  $Z_1 = 27$  where  $Z_1/Z_2 \sim 1$  and they level off above  $Z_1 = 54$ . These two features may be associated with the occurrence of maxima in the cross sections for target  $K$ -electron capture to the projectile  $K$ -shell around  $Z_1 = 30$  and to the projectile  $L$  shell around  $Z_1 = 60$  (see Fig. 11). Comparing the measured cross sections with the theoretical cross sections, it is again seen that good agreement is achieved for Ne and Ar projectiles, but beyond Ar the theoretical cross sections rapidly become much larger than the experimental cross sections. For Bi projectiles, the theoretical cross section is a factor of 18 larger than the experimental cross section. Moreover, it is evident from the curve shown in Fig. 13 that the data fall far below a  $Z_1^2$  scaling law beyond  $Z_1 = 24$ .

## V. CONCLUSIONS

Cross sections for  $K$ -vacancy production in Cu targets by 10-MeV/u projectiles of Ne, Ar, Cr, Kr, Xe, and Bi were determined from measured  $K$  x-ray yields. An analysis of the

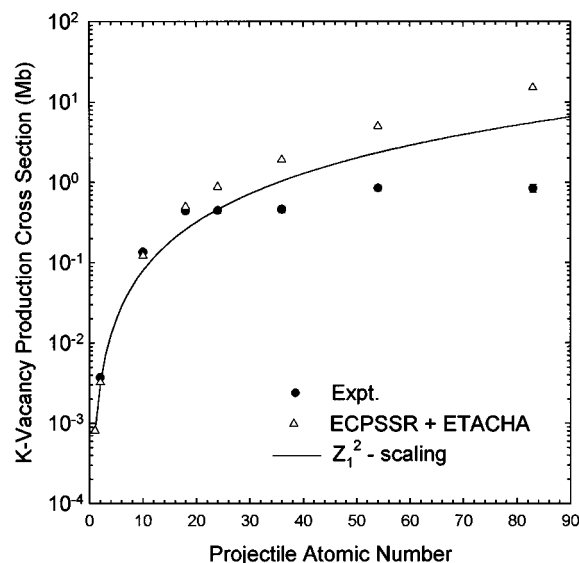


FIG. 13. Comparison of the  $K$ -shell vacancy production cross sections for equilibrated projectiles with theoretical (ECPSSR + ETACHA) total cross sections that have been averaged over target thickness. The measured data point for He ions is from Ref. [28].

Cu  $K\beta$ -to- $K\alpha$  intensity ratios resulting from heavy-ion excitation indicated that the multiply ionized states contributing to  $K$  x-ray emission are not statistically populated. High-resolution measurements were performed to establish the average numbers of target-atom  $L$ - and  $M$ -shell vacancies produced in  $K$ -shell ionizing collisions. This information was used to calculate the appropriate fluorescence yields for transforming the x-ray yields to vacancy production cross sections. The average  $L$ -shell vacancy production probability for  $K$ -shell ionizing collisions ( $p_L$ ) rose rapidly at low  $Z_1$ , but leveled off and approached a limiting value of about 0.59 at high  $Z_1$ . In addition, the high-resolution spectra revealed the presence of substantial contributions to the  $KL^0$  peak intensity from mechanisms other than those involving direct interactions with the projectile ions. It was found that photoionization of Cu atoms by Cu  $K\beta$  x rays produced in ion-atom collisions and shifted above the  $K$  absorption edge by multiple ionization accounted for the  $KL^0$  enhancements observed with Ne, Ar, and Cr ions. However, calculated photoionization yields were unable to fully account for the enhancements observed with Kr, Xe, and Bi ions. It was concluded, therefore, that another mechanism in addition to photoionization, probably ionization by secondary electrons, begins to contribute to this effect as the projectile atomic number rises above the target atomic number (i.e., in collision systems for which  $Z_1/Z_2 > 1$ ). In the case of Bi projectiles, the total  $KL^0$  enhancement was 23% of the total  $K\alpha$  x-ray intensity with only 57% of it being attributable to photoionization by target  $K\beta$  x rays and projectile  $L$  x rays.

Analysis of the thickness dependence of the Cu  $K$ -shell vacancy production cross sections provided the direct-ionization cross sections for zero-target thickness and the total  $K$ -electron-capture cross sections for equilibrated projectiles. The experimental direct-ionization cross sections and those predicted by the ECPSSR theory are in good agreement for Ne and Ar ions, but the theoretical cross sections rapidly diverge above the experimental values beyond

$Z_1=18$ . The experimental total-capture cross sections, however, were found to be in overall good agreement with those calculated for excited-state distributions predicted by the ETACHA code using the ECPSSR formulation. The total  $K$ -shell vacancy production cross sections for equilibrated projectiles rather unexpectedly saturate above  $Z_1=54$ , while the theoretical cross sections rise above the experimental cross sections beyond  $Z_1=18$  and deviate from them by a factor of 18 at  $Z_1=83$ .

#### ACKNOWLEDGMENTS

This work was supported by the Robert A. Welch Foundation. We thank Chris McFarland for help with the data analysis.

#### APPENDIX: CALCULATION OF THE PHOTOIONIZATION ENHANCEMENT RATIO

The procedure used to calculate the contribution to the  $KL^0$  peak from Cu  $K\alpha$  x rays produced as a result of the photoionization of Cu  $K$  electrons by photons excited in ion-atom collisions is outlined herein. In the particular cases of interest, the source photons arise from energy shifted Cu  $K\beta$  transitions in multiply ionized atoms and projectile x rays. It is assumed that the angles between the target surface normal and the detector axis, and the target surface normal and the beam axis are equal.

The photoionization  $KL^0$  enhancement ratio may be written as

$$R_E = I_p / I_{\text{tot}}, \quad (\text{A1})$$

where  $I_p$  is the observed intensity of  $KL^0$  x rays produced by photoionization and  $I_{\text{tot}}$  is the total observed  $K\alpha$  intensity (including the  $K\alpha$  satellites). The quantity  $I_p$  is given by

$$I_p = N_s \gamma T(\Omega\epsilon), \quad (\text{A2})$$

where  $N_s$  is the intensity of emitted source photons,  $\gamma$  is the probability that a Cu  $K\alpha$  x ray will be produced via photoionization by a source photon,  $T$  is the probability that a Cu  $K\alpha$  x ray will be transmitted out of the target over a path length determined by the effective thickness of the target as viewed by the x-ray detector, and  $(\Omega\epsilon)$  is the Cu  $K\alpha$  x-ray detection probability. The quantities  $N_s$  and  $\Omega\epsilon$  are measured, and assuming the Cu x rays are produced uniformly along the beam path (the length of which is the same as the distance these x rays must penetrate to reach the detector), the transmission probability is given by

$$T = \frac{1}{\mu t'} (1 - e^{-\mu t'}), \quad (\text{A3})$$

where  $\mu$  is the mass absorption coefficient and  $t'$  is the target thickness corrected for the target tilt angle.

Calculation of  $\gamma$ , the x-ray production probability, may be accomplished as follows. Consider a target of thickness  $t$  with surface normal at angle  $\alpha$  relative to the ion-beam axis, making its effective thickness  $t' = t(\cos \alpha)^{-1}$ . The probability that a source photon produced at depth  $x$  along the beam path escapes the target *without* photoionizing a target  $K$  electron is

$$p(x) = \int_0^\pi P(\theta) T_K(\theta, x) d\theta, \quad (\text{A4})$$

where  $P(\theta)d\theta$  is the probability that the photon is emitted between the angles  $\theta$  and  $\theta+d\theta$  measured relative to the surface normal, given by

$$P(\theta)d\theta = 1/2 \sin \theta d\theta \quad (\text{A5})$$

for an isotropic distribution and  $T_K$  is the transmission probability of the photon, given by

$$T_K(\theta, x) = e^{-\mu_K \tau(\theta, x)}. \quad (\text{A6})$$

In Eq. (A6),  $\mu_K$  is the mass absorption coefficient for  $K$ -shell photoionization and

$$\tau(\theta, x) = \begin{cases} (t-x \cos \alpha)/\cos \theta & \text{for } 0 \leq \theta < \pi/2 \\ x \cos \alpha / \cos \theta & \text{for } \pi/2 < \theta \leq \pi. \end{cases} \quad (\text{A7})$$

Finally, the x-ray production probability is obtained by numerical integration of the formula

$$\gamma = \omega_{K\alpha} \left[ 1 - \frac{1}{t'} \int_0^{t'} p(x) dx \right], \quad (\text{A8})$$

where  $\omega_{K\alpha}$  is the  $K\alpha$  fluorescence yield.

Equation (A2) also may be applied to the calculation of the intensity of Cu  $K\alpha$  x rays produced by projectile x rays that are emitted as the projectile passes through the target backing. In this case, however, Eq. (A4) reduces to

$$p = \frac{1}{2} + \int_{\pi/2}^\pi P(\theta) T_K(\theta) d\theta, \quad (\text{A9})$$

with

$$T_K(\theta) = e^{-\mu_K t' / \cos \theta}, \quad (\text{A10})$$

and Eq. (A8) becomes

$$\gamma = \omega_{K\alpha} (1 - p). \quad (\text{A11})$$

- [1] G. Lapicki, J. Phys. Chem. Ref. Data **18**, 111 (1989).  
 [2] W. Brandt and G. Lapicki, Phys. Rev. A **23**, 1717 (1981).  
 [3] G. Lapicki and F. D. McDaniel, Phys. Rev. A **23**, 975 (1981).  
 [4] T. J. Gray, P. Richard, R. L. Kauffman, T. C. Holloway, R. K. Gardner, G. M. Light, and J. Guertin, Phys. Rev. A **13**, 1344

(1976).

- [5] R. K. Gardner, T. J. Gray, P. Richard, C. Schmiederkamp, K. A. Jamison, and J. M. Hall, Phys. Rev. A **19**, 1896 (1979).  
 [6] R. Anholt, W. E. Meyerhof, Ch. Stoller, E. Morenzoni, S. A. Andriamonje, J. D. Molitoris, O. K. Baker, D. H. H. Hoff-

- mann, H. Bowman, J.-S. Xu, Z.-Z. Xu, K. Frankel, D. Murphy, K. Crowe, and J. O. Rasmussen, *Phys. Rev. A* **30**, 2234 (1984).
- [7] J. A. Tanis, S. M. Shafroth, W. W. Jacobs, T. McAbee, and G. Lapiki, *Phys. Rev. A* **31**, 750 (1985).
- [8] E. Liatard, J. F. Bruandet, F. Glasser, T. U. Chan, G. J. Costa, C. Gérardin, C. Heitz, M. Samri, and R. Seltz, *Z. Phys. D* **2**, 223 (1986).
- [9] V. Horvat, G. Sampoll, K. Wohrer, M. Chabot, and R. L. Watson, *Phys. Rev. A* **46**, 2572 (1992).
- [10] L. C. Tribedi, K. G. Prasad, and P. N. Tandon, *Phys. Rev. A* **47**, 3739 (1993).
- [11] L. C. Tribedi, K. G. Prasad, P. N. Tandon, Z. Chen, and C. D. Lin, *Phys. Rev. A* **49**, 1015 (1994).
- [12] D. Mitra, M. Sarkar, D. Bhattacharya, P. Sen, G. Kuri, and G. Lapicki, *Nucl. Instrum. Methods Phys. Res. B* **124**, 453 (1997).
- [13] J. D. Garcia, R. J. Fortner, and T. M. Kavanagh, *Rev. Mod. Phys.* **45**, 111 (1973); P. Richard, in *Atomic Inner-Shell Processes*, edited by B. Crasemann (Academic, New York, 1975), Vol. I; R. K. Gardner and T. J. Gray, *At. Data Nucl. Data Tables* **21**, 515 (1978).
- [14] T. J. Gray, P. Richard, G. Gealy, and J. Newcomb, *Phys. Rev. A* **19**, 1424 (1979).
- [15] J. P. Rozet, C. Stéphan, and D. Vernhet, *Nucl. Instrum. Methods Phys. Res. B* **107**, 67 (1996).
- [16] Goodfellow, 800 Lancaster Avenue, Berwyn, PA 19312.
- [17] Chromium Corporation, 8701 Union Avenue, Cleveland, OH 44105.
- [18] Amptek, Inc., 6 De Angelo Drive, Bedford, MA 01730.
- [19] G. J. Pedrazzini, J. Pálinkás, R. L. Watson, D. A. Church, and R. A. Kenefick, *Nucl. Instrum. Methods Phys. Res. B* **10/11**, 904 (1985).
- [20] G. Hölzer, M. Fritsch, M. Deutsch, J. Härtwig, and E. Förster, *Phys. Rev. A* **56**, 4554 (1997).
- [21] J. P. Desclaux, *Comput. Phys. Commun.* **9**, 31 (1975).
- [22] R. L. Watson, F. E. Jenson, and T. Chiao, *Phys. Rev. A* **10**, 1230 (1974).
- [23] A. R. Knudson, P. G. Burkhalter, and D. J. Nagel, *Atomic Collisions in Solids*, edited by S. Datz, B. R. Appleton, and C. D. Moak (Plenum, New York, 1975), p. 421.
- [24] L. Schleinkofer, F. Bell, E. Spindler, and H.-D. Betz, *J. Phys. B* **11**, L451 (1978).
- [25] J. H. Scofield, *Phys. Rev. A* **9**, 1041 (1974).
- [26] M. H. Chen, B. Crasemann, and H. Mark, *At. Data Nucl. Data Tables* **24**, 13 (1979).
- [27] F. P. Larkins, *J. Phys. B* **4**, L29 (1971).
- [28] T. L. Hardt and R. L. Watson, *Phys. Rev. A* **7**, 1917 (1973).